Journal of Hydroscience and Hydraulic Engineering
Vol. 19, No.2 November, 2001, 85-92

Direct Numerical Simulation of Turbulence Over Two-Dimensional Dunes Using CIP Method

By

Yasuyuki Shimizu
Associate Professor, Department of Civil Engineering,
Hokkaido University, Sapporo, Japan,

Mark.W. Schmeeckle
Associate Professor, Department of Geophisics,
Florida State University, USA

and

Jonathan M. Nelson
US Geological Survey, USA

SYNOPSIS

The finite amplitude growth and stability of ripples and dunes is believed to be the result of the interaction between the complex turbulence field induced by separation at the crest of the bed feature and bedload sediment transport. Numerical simulation of this turbulence field promises to provide the detailed qualitative and quantitative information of coherent structures that is required to model the sediment transport field over ripples and dunes. We present a high-order Godunov scheme, referred to as the CIP method, for the numerical simulation of turbulence over a 2-dimensional dune. This method splits the integration of the Navier-Stokes equations into a non-advection and pure advection phases. The solution of the non-advection phase is cubically interpolated and then advected to the solution grid points. Comparison of the velocity statistics of the numerical simulation with LDV measurements over 2-dimensional dunes in a flume is favorable. Analysis of the vorticity field reveals that the coherent turbulent structures produced in the shear layer are highly three-dimensional, and cross-stream velocities should be considered in future models of bedload transport over dunes.

Keywords: dune, CIP method, LDV, numerical model, turbulence

INTRODUCTION

The sediment transport field over dunes and ripples in open-channel flows is strongly affected by the complex turbulence field caused by flow separation at the dune crest. The influence of flow separation due to a chance piling up of a number of grains has long been invoked as the mechanism by which sand waves initially form [Inglis(1), Raudkivi,(2), Williams and Kemp(3)]. Bedload sediment transport at low and moderate transport stages is highly intermittent, with the largest portion of transport taking place during sweep events. The frequency, duration, spatial scale, and magnitude of sweep events are critical to determining the average bedload sediment transport rate. Nelson et al.(4) made simultaneous high-frequency measurements of near-bed velocity and bedload sediment transport rate downstream of a backward step, and found a sharp downstream peak in the sediment transport rate even though the boundary shear stress was nearly flat in the same area. Gry and Schmid(5) made simultaneous observations of sediment transport and near-bed velocity on an initially flat bed, and found that initial bedforms formed in response to sweep structures. Measurements of near-bed velocity over fixed dunes indicate that the statistics of sweep events are very different from that in an uniform turbulent boundary layer with the same local boundary shear stress [Bennet and Best(6), McLean et al.(7)]. A detailed understanding of the interaction between separation-produced turbulent structures and bedload sediment transport is required to understand the finite amplitude growth and stability of ripples and dunes.

Two parts are needed to solve the bedload sediment transport field over dunes. The first is a model which can calculate the bedload transport rate as a function of the complex spatially and temporally varying near-bed velocity field, and it must be particularly capable of calculating the transport during sweep events. Such a model, based on the direct simultaneous numerical integration of all particles in a bed, driven by a temporally and spatially variable imposed near-bed velocity, has been produced [Schmeeckle8), Schmeeckle et. al9)]. The second part needed to solve the bedload transport over dunes is the near-bed velocity field itself. Traditional velocimetry methods, such as hot-wire, laser Doppler, and acoustic Doppler, can only measure the velocity of a single small sample volume, and, hence, cannot provide high-frequency velocity measurements over a broad area. Imaging techniques such as particle tracking, PTV, and particle image velocimetry, PIV, can provide high-frequency, whole-field velocity measurements, but there is generally a trade-off between accuracy and the size of the field to be measured, and the data is generally two-dimensional. Numerical simulations of turbulence promise to provide high-frequency velocity fields over large areas in three dimensions. Also, the geometry of a numerical simulation can be easily changed to provide turbulence data for a whole suite of geometries. In this paper we present a numerical simulation of turbulence over two-dimensional dunes and compare the results to a set of flume experiments.

BASIC EQUATIONS

In a numerical simulation of turbulence, we seek to solve the Navier-Stokes equations and the incompressible continuity equation without further simplifying assumptions.

$$\frac{D\vec{U}}{Dt} = -\frac{1}{\rho}\vec{\nabla}p + \nu\nabla^2\vec{U} + \vec{g} \tag{1}$$

$$\vec{\nabla}\cdot\vec{U} = 0 \tag{2}$$

in which U is velocity, p is pressure, ρ is fluid density, g is acceleration of gravity, and ν is kinematic viscosity.

For a direct numerical simulation, DNS, of turbulence, the grid spacing must be as small as the dissipation length scales so that the natural cascade of energy from the large eddies to viscous dissipation at very small scales can be modeled. This requires a very fine mesh and many days, if not weeks, on the fastest current supercomputers for high Reynolds number flows. The usual alternative is to use large eddy simulations, LES, whereby the subgrid stresses are modeled, rather than being directly calculated. Neto et al.10) performed simulations of flow downstream of a backward step using several subgrid stress models and some simulations with no subgrid model. Comparison of calculations with and without a subgrid model reveals that the turbulence intensity in the no-subgrid simulations are somewhat high, however the coherent structures generated in the shear layer are nearly the same as those of the subgrid simulations. For the calculations herein, we use no subgrid model. Calculations of this type are generally referred to as Euler simulations.

The equations are transformed from an x, y, z cartesian coordinate system to a boundary fitted x, y, ζ coordinate system by the following equation.

$$\zeta = \frac{H-z}{h} \tag{3}$$

in which x, y, and z are in the downstream, cross-stream, and vertical directions, respectively. H is water surface elevation ($= \eta + h$), η is bed elevation, and h is local flow depth. Applying this coordinate transformation to Equations (1) and (2) results in the following:

$$\frac{\partial u}{\partial t} + u\frac{\partial u}{\partial x} + v\frac{\partial u}{\partial y} + \frac{w_2}{h}\frac{\partial u}{\partial \zeta} = -g\frac{\partial H}{\partial x} - g\frac{\partial h'}{\partial x} + g\frac{\partial \Omega}{h}\frac{\partial h'}{\partial \zeta} + \nu\Delta u \tag{4}$$

$$\frac{\partial v}{\partial t} + u\frac{\partial v}{\partial x} + v\frac{\partial v}{\partial y} + \frac{w_2}{h}\frac{\partial v}{\partial \zeta} = -g\frac{\partial H}{\partial y} - g\frac{\partial h'}{\partial y} + g\frac{\partial \Psi}{h}\frac{\partial h'}{\partial \zeta} + \nu\Delta v \tag{5}$$

$$\frac{\partial w}{\partial t} + u\frac{\partial w}{\partial x} + v\frac{\partial w}{\partial y} + \frac{w_2}{h}\frac{\partial w}{\partial \zeta} = -\frac{g}{h}\frac{\partial h'}{\partial \zeta} + \nu\Delta w \tag{6}$$

$$\frac{\partial (hu)}{\partial x} + \frac{\partial (hv)}{\partial y} + \frac{\partial w_1}{\partial \zeta} = 0 \tag{7}$$

in which,

$$w_1 = w - u\Omega - v\Psi \tag{8}$$

$$\Omega = \frac{\partial \eta}{\partial x} + \zeta\frac{\partial h}{\partial x} \tag{9}$$

$$\Psi = \frac{\partial \eta}{\partial y} + \zeta\frac{\partial h}{\partial y} \tag{10}$$

$$w_2 = w_1 - \zeta\frac{\partial H}{\partial t} \tag{11}$$

$$p = p_0 + p' = \rho g(H - z) + \rho g h' \tag{12}$$

$$\Delta = \frac{\partial^2}{\partial x^2} + \frac{\partial^2}{\partial y^2} + \frac{1}{h^2}\frac{\partial^2}{\partial \zeta^2} - \frac{2\Omega}{h}\frac{\partial^2}{\partial x \partial \zeta} - \frac{2\Psi}{h}\frac{\partial^2}{\partial y \partial \zeta}$$

$$-\frac{1}{h}\left(\frac{\partial \Omega}{\partial x} + \frac{\partial \Psi}{\partial y} - \frac{2\Omega}{h}\frac{\partial h}{\partial x} - \frac{2\Psi}{h}\frac{\partial h}{\partial y}\right)\frac{\partial}{\partial \zeta} \tag{13}$$

p' is the non-hydrostatic component of pressure, and $h' = p'/(\rho g)$.

The boundary conditions are the no slip condition at the bed, frictionless sidewalls and an unstressed upper surface: $u = v = w = h' = 0$ at the channel bed. $\partial u/\partial y = \partial w/\partial \zeta = v = h' = 0$ at the side walls. $\partial u/\partial \zeta = \partial v/\partial y = h' = 0$ at the water surface. Initially, v, w, and h' are set to zero, and a logarithmic structure is specified for u to take into account for the effect of skin friction roughness of the bed. The effect of friction of side walls are neglected because the side walls are very smooth glasses. The input at the upstream end is set as the output at the downstream end. The effect of time dependent change of water surface elevation is neglected and it is kept constant in this model. At the beginning of the calculation the flow quickly becomes unstable and after several flow-through time intervals the turbulence statistics become stable.

NUMERICAL PROCEDURE

To solve the equations we use a high-order Godunov scheme known as the cubic interpolated psuedo-particle, CIP, method proposed by Yabe and co-workers [Yabe and Takei[11], Yabe et al. [12]]. The assumption is made that at very small time increments the change in time of the velocity components at a point in space can be broken down into the time evolution of the inhomogeneous terms and the time evolution at a point due to the advection of the field. So, in the first step the change in time of the velocity is solved as:

$$\frac{\partial f^*}{\partial t} = G \tag{14}$$

in which f is u, v and w, G is the right-hand side of Eqs. 4-6. Then f is solved in the advection phase as

$$\frac{\partial f}{\partial t} + u\frac{\partial f}{\partial x} + v\frac{\partial f}{\partial y} + \frac{w_2}{h}\frac{\partial f}{\partial \zeta} = 0 \tag{15}$$

Whose solution for small Δt is simply approximated as:

$$f(x, y, \zeta, t + \Delta t) \approx f(x - u\Delta t, y - v\Delta t, \zeta - \frac{w_2}{h}\Delta t, t) \tag{16}$$

Using the solution of the non-advection phase (Eq. 14), the approximation becomes

$$f(x, y, \zeta, t + \Delta t) \approx f^*(x - u\Delta t, y - v\Delta t, \zeta - \frac{w_2}{h}\Delta t, t + \Delta t) \tag{17}$$

The trick then is to find the value of f^* at points in space, which generally do not lie on the numerical grid points, as specified by the right hand side of Eq. 17. If linear interpolation is used to find f^* at points not on the grid, the first order Godunov method is attained. A more accurate solution requires higher order interpolation, and thus high-order Godunov schemes. In the CIP method, a cubic interpolation of f^* is proposed, and when the interpolation is combined with Eq. 17 the resultant equation for f at grid point, i, j, k and time $n + 1$ is given by:

$$f^{n+1}_{i,j,k} = \left[(a_1 x_0 + a_4 y_0 + a_7 \zeta_0 + a_{11}) x_0 + a_{14} y_0 + \partial_x f^*_{i,j,k}\right] x_0$$

$$+ \left[(a_2 y_0 + a_5 x_0 + a_8 \zeta_0 + a_{12}) y_0 + a_{15} \zeta_0 + \partial_y f^*_{i,j,k}\right] y_0$$

$$+ \left[(a_3 y_0 + a_6 x_0 + a_9 y_0 + a_{13}) \zeta_0 + a_{16} x_0 + \partial_\zeta f^*_{i,j,k}\right] \zeta_0 + a_{10} x_0 y_0 \zeta_0 + f^*_{i,j,k} \tag{18}$$

in which,

$$x_0 = -u\Delta t, \quad y_0 = -v\Delta t, \quad \zeta_0 = -\frac{w_2}{h}\Delta t \tag{19}$$

$$\partial_x f = \frac{\partial f}{\partial x}, \quad \partial_y f = \frac{\partial f}{\partial y}, \quad \partial_\zeta f = \frac{\partial f}{\partial \zeta} \tag{20}$$

$$a_1 = [(\partial_x f^*_{i,j,k} + \partial_x f^*_{i+1,j,k})\Delta x + 2(f^*_{i,j,k} - f^*_{i+1,j,k})]/\Delta x^3 \tag{21}$$

$$a_2 = [(\partial_y f^*_{i,j,k} + \partial_y f^*_{i,j+1,k})\Delta y + 2(f^*_{i,j,k} - f^*_{i,j+1,k})]/\Delta y^3 \tag{22}$$

$$a_3 = [(\partial_\zeta f^*_{i,j,k} + \partial_\zeta f^*_{i,j,k+1})\Delta\zeta + 2(f^*_{i,j,k} - f^*_{i,j,k+1})]/\Delta\zeta^3 \tag{23}$$

$$a_4 = [b_1 - (-\partial_x f^*_{i,j,k} + \partial_x f^*_{i,j+1,k})\Delta x]/\Delta x^2\Delta y \tag{24}$$

$$a_5 = [b_1 - (-\partial_y f^*_{i,j,k} + \partial_y f^*_{i+1,j,k})\Delta y]/\Delta x\Delta y^2 \tag{25}$$

$$a_6 = [b_3 - (-\partial_\zeta f^*_{i,j,k} + \partial_\zeta f^*_{i+1,j,k})\Delta\zeta]/\Delta x\Delta\zeta^2 \tag{26}$$

$$a_7 = [b_3 - (-\partial_x f^*_{i,j,k} + \partial_x f^*_{i,j,k+1})\Delta x]/\Delta x^2\Delta\zeta \tag{27}$$

$$a_8 = [b_2 - (-\partial_y f^*_{i,j,k} + \partial_y f^*_{i,j,k+1})\Delta y]/\Delta y^2\Delta\zeta \tag{28}$$

$$a_9 = [b_2 - (-\partial_\zeta f^*_{i,j,k} + \partial_\zeta f^*_{i,j+1,k})\Delta\zeta]/\Delta y\Delta\zeta^2 \tag{29}$$

$$\begin{gathered} a_{10} = [-f^*_{i,j,k} + (f^*_{i+1,j,k} + f^*_{i,j+1,k} + f^*_{i,j,k+1}) \\ -(f^*_{i+1,j+1,k} + f^*_{i,j+1,k+1} + f^*(i+1,j,k+1)) + f^*_{i+1,j+1,k+1}]/\Delta x\Delta y\Delta\zeta \end{gathered} \tag{30}$$

$$a_{11} = [3(f^*_{i+1,j,k} - f^*_{i,j,k}) - (\partial_x f^*_{i+1,j,k} + 2\partial_x f^*_{i,j,k})\Delta x]/\Delta x^2 \tag{31}$$

$$a_{12} = [3(f^*_{i,j+1,k} - f^*_{i,j,k}) - (\partial_y f^*_{i,j+1,k} + 2\partial_x f^*_{i,j,k})\Delta y]/\Delta y^2 \tag{32}$$

$$a_{13} = [3(f^*_{i,j,k+1} - f^*_{i,j,k}) - (\partial_\zeta f^*_{i,j,k+1} + 2\partial_\zeta f^*_{i,j,k})\Delta\zeta]/\Delta\zeta^2 \tag{33}$$

$$a_{14} = [-b_1 + (-\partial_x f^*_{i,j,k} + \partial_x f^*_{i,j+1,k})\Delta x + (-\partial_y f^*_{i,j,k} + \partial_y f^*_{i+1,j,k})\Delta y]/\Delta x\Delta y \tag{34}$$

$$a_{15} = [-b_2 + (-\partial_y f^*_{i,j,k} + \partial_y fi,j,k+1))\Delta y + (-\partial_\zeta f^*_{i,j,k} + \partial_\zeta f^*_{i,j+1,k})\Delta\zeta]/\Delta y\Delta\zeta \tag{35}$$

$$a_{16} = [-b_3 + (-\partial_\zeta f^*_{i,j,k} + \partial_\zeta f^*_{i+1,j,k})\Delta\zeta + (-\partial_x f^*_{i,j,k} + \partial_x f^*_{i,j,k+1})\Delta x]/\Delta x\Delta\zeta \tag{36}$$

$$b_1 = f^*_{i,j,k} - f^*_{i+1,j,k} - f^*_{i,j+1,k} + f^*_{i+1,j+1,k} \tag{37}$$

$$b_2 = f^*_{i,j,k} - f^*_{i,j+1,k} - f^*_{i,j,k+1} + f^*_{i,j+1,k+1} \tag{38}$$

$$b_3 = f^*_{i,j,k} - f^*_{i+1,j,k} - f^*_{i,j,k+1} + f^*(i+1,j,k+1) \tag{39}$$

In the above instance it is assumed that u, v, and w_2/h are all negative, so that the advection to the grid point, (i,j,k), is from within the volume whose vertices are (i,j,k), $(i+1,j,k)$, $(i,j+1,k)$, $(i,j,k+1)$, $(i+1,j+1,k)$, $(i+1,j,k+1)$, $(i,j+1,k+1)$, and $(i+1,j+1,k+1)$. When $u \geq 0$, the index, $i+1$, in Eqs. 21-39 should be changed to $i-1$, and Δx goes to $-\Delta x$. Similarly, when $v \geq 0$, $j+1$ and Δy becomes $j-1$ and $-\Delta y$, and when $w_2/h \geq 0$, $k+1$ and $\Delta\zeta$ becomes $k-1$ and $-\Delta\zeta$, respectively.

In the non-advection phase, f^* is calculated with the continuity equation by taking the divergence of the momentum equations and solving for pressure as a Poisson equation. The viscous terms are approximated using central differences. Each velocity component is defined on the center of two faces of the computational cells, and pressure is defined at the center of the cell.

At first f^* is calculated from Eq. 14 in which the convective acceleration terms do not appear. In the second phase, f is calculated at the grid points from a pure advection of the cubic interpolated field of f^* by Equations 18-39. These two steps complete the calculation of a single time increment, Δt. The CIP method has been shown to solve the problem of boundedness while introducing little numerical diffusion, and algorithm implementation is more straightforward than other high-order upwind schemes.

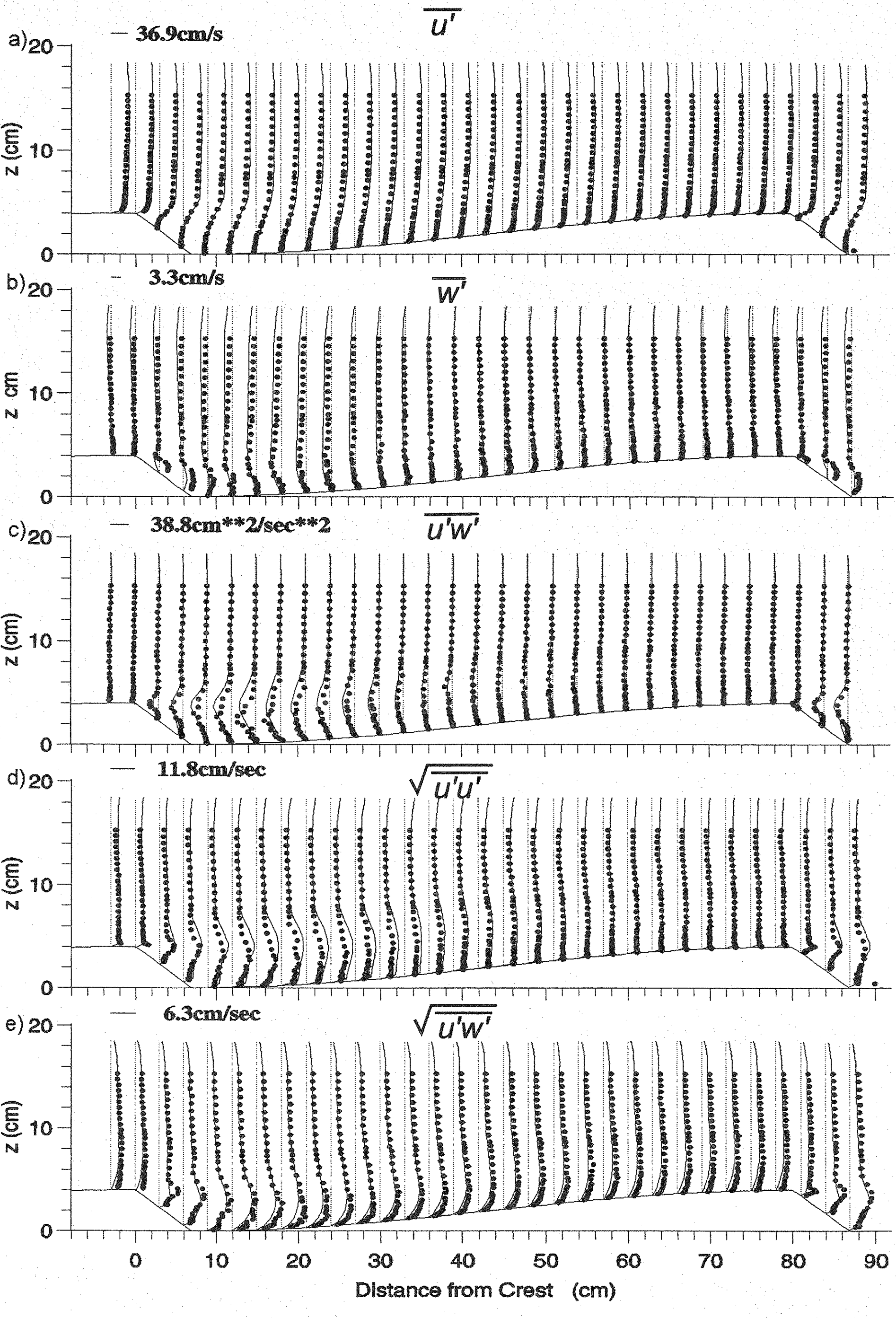

Fig.1 Comparison of turbulence statistics between numerical simulation and experiments.

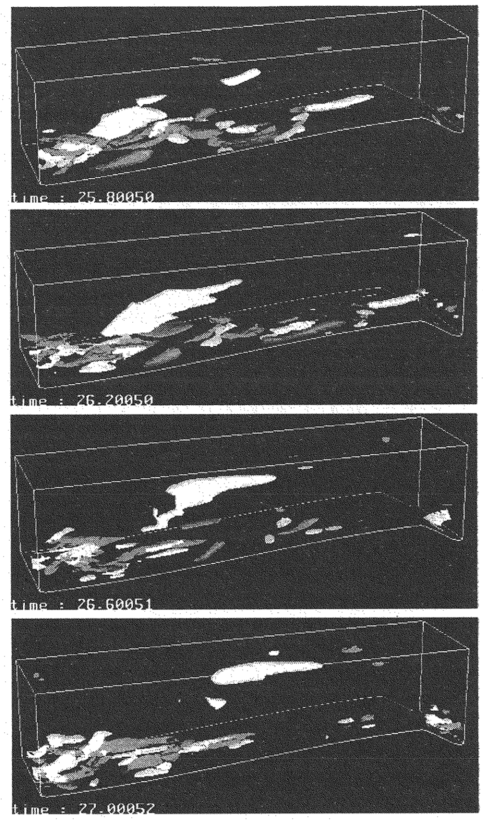

Fig.2: Downstream isovorticity surfaces $\partial w/\partial y - \partial v/\partial z$ for positive (white) and negative (gray) $8s^{-1}$. Each of the four plots are separated by 0.4 seconds.

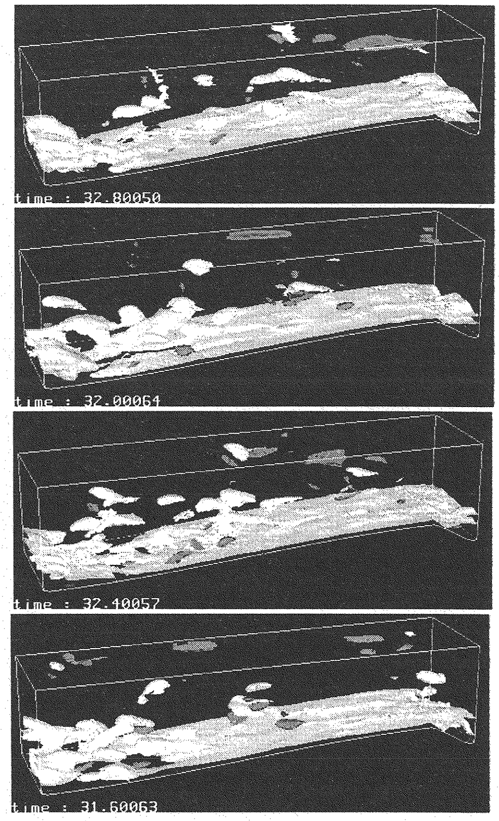

Fig.3: Crossstream isovorticity surfaces $\partial u/\partial z - \partial w/\partial x$ for positive (white) and negative (gray) $10s^{-1}$. Each of the four plots are separated by 0.4 seconds

RESULTS

The conditions of the present simulation are identical to a set of experiments conducted in an open-channel water flume over 2-dimensional dunes. The dune dimensions were 80cm in length, 40cm width, and 4cm height from the lowest point in the trough to the dune crest. The shape of the dunes is the same as that of Nelson and Smith [13)] with a half sine wave forming the stoss of the dune and a 30 degree straight slip face from crest to trough (see Fig. 1). The average depth of flow and velocity of the experiments were 17cm and 31 cm/s. Well-sorted sand with an average diameter of 0.7mm was glued to the dune forms to provide roughness. A laser Doppler velocimeter was used to measure two components of velocity, in the downstream and vertical directions. The measurements were taken over a dune of which six dunes were placed upstream and two downstream. The geometry of the numerical simulation was identical to that of the experiment except that the channel width was set to 20cm in order to decrease the length of the computations. Computational grid numbers in one dune length were 322, 40 and 34 in x, y and ζ directions, respectively. Fig. 1 shows comparison between the numerical and experimental results. The mean downstream and vertical velocities are agree well with the data, respectively. The Reynolds stress, $-\rho\overline{u'w'}$, in the separation shear layer is also modeled well. Although, there is a systematic deviation in the position of the shear layer just several dune heights downstream of the crest. The shear layer stress profile is shifted more into the interior of the flow than is the experimental results. This slight vertical shift can also be seen in the root mean square velocities.

Figs. 2 and 3 are four sequential pictures of vorticity isosurfaces each separated by 0.4 seconds. Fig. 2 is the vorticity in the downstream direction, $\partial w/\partial y - \partial v/\partial z$, and Fig. 3 is the vorticity in the cross-stream direction, $\partial u/\partial z - \partial w/\partial x$. Separation results in a shear layer which quickly becomes three-dimensional. Strong downstream vortices, which are generally but not always paired as counter-rotating vortices, appear in the separation bubble and persist downstream until about half way up the stoss side of the bedform. A downstream or cross-stream vortex will intermittently detach from the near bed region and rise to the surface as shown by the sequence in Fig. 2. Another feature, which is readily apparent, is that the strong vortices depicted by these isovorticity surfaces rarely extend beyond the upstream half of the stoss side of the bed. In contrast, the backward step simulations of Neto et al.10) show that the downstream vortices persist with little diminishment to the downstream end of their computational domain twelve step heights downstream.

SUMMARY AND CONCLUSION

A method was presented for the numerical simulation of turbulence over 2-dimensional dunes by applying the CIP method to solve the Navier-Stokes equations. Resulting turbulence statistics compare favorably with experimental results. These model results show that the coherent structures downstream of the dune crest are highly three-dimensional, with the size and strength of downstream vortices being comparable to the cross-stream vortices generated by Kelvin-Helmholtz instabilities in the shear layer. This suggests that future studies on the motion of bedload particles on the stoss of bedforms should consider the role of cross-stream near-bed velocities in enhancing initiation of motion and transport during sweep events.

REFERENCES

(1) Inglis, C.C.: The behavior and control of rivers and canals, *Research Publication No. 13 Central Water Power*, Irrigation and Navigation Research Station, Poona, India, Part II, 1949.
(2) Raudkivi, A.J.: Study of ripple formation, *Journal of the Hydraulics Division*, ASCE, 89, 1963.
(3) Williams, P.B. and P.H. Kemp: Initiation of ripples on flat sediment beds, *Journal of the Hydraulics Division*, Proceedings of the American Society of Civil Engineers, 97, 505–522, 1971.
(4) Nelson, J.M., R.L. Shreve, S.R. McLean, and T.G. Drake: Role of near-bed turbulence structure in bedload transport and bedform mechanics, *Water Resources Research*, 31, 2071–2086, 1995.
(5) Gyr, A. and A. Schmid: Turbulent flows over smooth erodible sand beds in flumes, *Journal of Hydraulic Research*, 35, 525–544, 1997.
(6) Bennet, S.J. and J.L. Best: Mean flow and turbulence structure over fixed, two-dimensional dunes; implications for sediment transport and bedform stability, *Sedimentology*, 42, 491–513, 1995.
(7) McLean, S.R., J.M. Nelson, and S.R. Wolfe: Turbulence structure over two-dimensional bedforms, *Journal of Geophysical Research*, 12, 729–747, 1994.
(8) Schmeecle, M.W.: A dynamic boundary condition for bedload sediment transport in non-uniform, hydraulically rough turbulent boundary layers, *Annual Journal of Hydraulic Engineering*, Vol.42, JSCE, 653–658, 1999.
(9) Schmeecle, M.W., J.M. Nelson, and J. Pitlick: Direct numerical simulation of bedload sediment transport: In H. Murakami and J.E. Luco, *12th ASCE Engineering Mechanics Conference Proceedings*, American Society of Civil Engineers, 1998.
(10) Neto, A. Silveira, D. Grand, O. Metais, and M. Lesieur: A numerical investigation of the coherent vortices in turbulence behind a backward-facing step, *Journal of Fluid Mechanics*, 256, 1–25, 1993.
(11) Yabe, T. and E. Takei, A new higher-order Godunov method for general hyperbolic equations, *Journal of the Physical Society of Japan*, 57, 2598–2601, 1988.
(12) Yabe, T., T. Ishikawa, Y. Kadota, and F. Ikeda: A multidimensional cubic-interpolated pseudoparticle (CIP) method without time splitting technique for hyperbolic equations, *Journal of the Physical Society of Japan*, 59, 2301–2304, 1990.
(13) Nelson, J.M. and J.Dungan Smith: Mechanics of flow over ripples and dunes, *Journal of Geophysical Research*, 94, 8146–8162, 1989.

APPENDIX – NOTATION

The following symbols are used in this paper:

H = water surface elevation;
$\vec{U}$ = velocity vector;
$a_1 \sim a_{16}$ = Eqs. 21–36;
$b_1 \sim b_3$ = Eqs. 37–39;
f = u, v and w;
f^* = value of f at non-advection phase;
g = acceleration of gravity;
$\vec{g}$ = acceleration vector;
h = depth;
h' = $p'/(\rho g)$;
p = pressure;
p' = non-hydrostatic component of pressure;
t = time;
u = velocity component in x-direction;
v = velocity component in y-direction;
w = velocity component in z-direction;
w_1 = Eq. 8;
w_2 = Eq. 11;
x = downstream direction;
y = cross stream direction;
z = vertical direction;
Ω = Eq. 9;
Ψ = Eq. 10;
Δ = Eq. 13;
ρ = fluid density;
ν = kinematic viscosity; and
ζ = $(H - z)/h$.

(Received September 1, 2000 ; revised April 12, 2001)